# Nanoscale

Accepted Manuscript


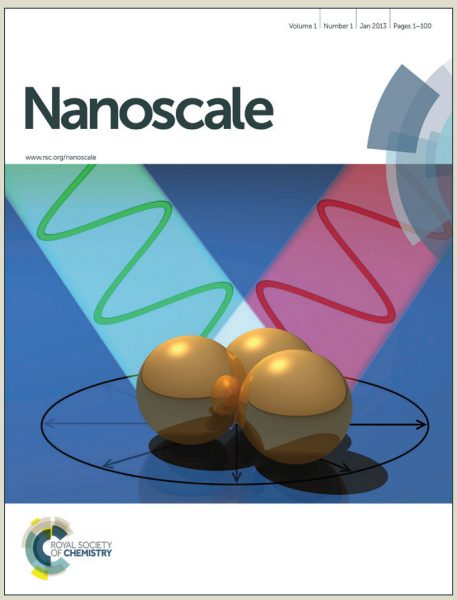





ROYAL SOCIETY OF CHEMISTRY

www.rsc.org/nanoscale

Cite this: DOI: 10.1039/c0xx00000x

www.rsc.org/xxxxxx

ARTICLE TYPE

# Preparation and enhanced visible light photocatalytic activity of novel g-$C_3N_4$ nanosheets loaded with $Ag_2CO_3$ nanoparticles

**Yunfeng Li,[a] Lin Fang,[a] Renxi Jin,[a] Yang Yang,[a] Xu Fang,[a] Yan Xing*[a] and Shuyan Song*[b]**

***Received (in XXX, XXX) Xth XXXXXXXXX 20XX, Accepted Xth XXXXXXXXX 20XX***

**DOI: 10.1039/b000000x**

As a potential visible-light photocatalyst, the photocatalytic performance of the bulk g-$C_3N_4$ synthesized by heating melamine (denote as g-$C_3N_4$-M) is limited due to its low specific surface area and the high recombination rate of photo-induced electron-hole pair. In this paper, a novel g-$C_3N_4$-M nanosheet (g-$C_3N_4$-MN) obtained from the bulk g-$C_3N_4$-M through a thermal exploitation method is employed to be an excellent substrate and the $Ag_2CO_3$ nanoparticles are loaded with different amount at room temperature. The phase and chemical structure, electronic and optical properties of $Ag_2CO_3$/g-$C_3N_4$-MN heterostructures are well-characterized. The photocatalytic activities of the as-prepared $Ag_2CO_3$/g-$C_3N_4$-MN are evaluated by the degradation of methyl orange (MO) and rhodamine B (RhB) pollutants under visible light irradiation. More importantly, $Ag_2CO_3$/g-$C_3N_4$-MN heterostructure has been proved to be an excellent photocatalytic system with an enhanced specific surface area and charge separation rate compared with those of the $Ag_2CO_3$/g-$C_3N_4$-M system.

## Introduction

In recent years, the design of efficient, simple and sustainable photocatalysts has received much attention owing to their potential value in worldwide energy shortage and environmental purification.[1,2] However, the most widely used photocatalyst, $TiO_2$, has limited practical applications due to its low solar energy conversion efficiency and the high recombination of photogenerated electron–hole pairs.[3-5] Therefore, it is very urgent to develop efficient visible-light-active photocatalysts. Recently, many new visible-light-responsive photocatalysts have been reported, such as $WO_3$,[6,7] CdS,[8,9] $BiVO_4$,[10,11] $Bi_2WO_6$,[12,13] and $Cu_2O$.[14,15] Among them, silver-containing compounds have been proved to be one of the most promising photocatalysts because of their high utilization rate of visible light. Typically, Yu *et al.* reported the simple hydrothermal synthesis of ultralong $Ag_2Mo_3O_{11}$ nanowires and their potential application in the degradation of organic contaminants RhB.[16] Moreover, it was reported that AgBr nanoplates with exposed {111} facets exhibited greatly enhanced photocatalytic properties for the degradation of organic pollutants.[17] Ye and co-workers recently reported that $Ag_3PO_4$ exhibited excellent photooxidative capabilities for $O_2$ evolution from water and organic dye decomposition under visible-light irradiation.[18,19] Notably, silver carbonate ($Ag_2CO_3$), as a novel high-efficiency visible-light-driven photocatalyst, has shown a high photocatalytic activity for the photodegradation of organic pollutant molecules.[20] Unfortunately, like most of other silver-containing photocatalysts, $Ag_2CO_3$ photocatalyst greatly suffers from poor stability under visible light due to the photocorrosion.[21] Yu *et al.* recently reported that the photocorrosion of $Ag_2CO_3$ could be efficiently inhibited by employing $AgNO_3$ as an electron acceptor in the photocatalytic reaction system.[22] Also Jin *et al.* have successfully synthesized $Ag_2O$/$Ag_2CO_3$ heterostructured photocatalyst to improve the photocatalytic activity and stability of $Ag_2CO_3$.[23] However, developing visible light photocatalysts with sufficient charge separation ability and high photocatalytic stability is still the most challenging task in photocatalysis research.

Graphite-like carbon nitride (g-$C_3N_4$), a kind of metal-free semiconductor material possessing a narrow band gap of 2.7 eV, has attracted much attention due to its high photocatalytic performance for water splitting[24] and the photo-degradation of organic pollutants[25] under visible light. However, the photocatalytic performance of g-$C_3N_4$ is still limited due to its high recombination rate of the photo-induced electron-hole pair and the low specific surface area. To advance this promising photocatalytic material, researchers have coupled g-$C_3N_4$ with various silver-containing compounds, such as Ag/g-$C_3N_4$,[26,27] g-$C_3N_4$/$Ag_2O$,[28] Ag/AgBr/g-$C_3N_4$,[29] g-$C_3N_4$/$Ag_3PO_4$[30] and g-$C_3N_4$/$Ag_2CO_3$[31] to increase the separation efficiency of photogenerated electrone-hole pairs, thus to improve the photocatalytic performance. However, as a kind of photocatalyst, the lower specific surface area of g-$C_3N_4$ is still not satisfying and the photocatalytic activity of g-$C_3N_4$-based photocatalysts may be further enhanced by increasing the specific surface area of g-$C_3N_4$.

In this work, g-$C_3N_4$-M nanosheet (g-$C_3N_4$-MN) obtained from the bulk g-$C_3N_4$-M through a thermal exploitation method[32,33] is used as an excellent substrate, and $Ag_2CO_3$ nanoparticles have been loaded on the surface of g-$C_3N_4$-M nanosheets with high dispersity. The as-prepared $Ag_2CO_3$/g-$C_3N_4$-MN nanocomposites exhibit enhanced visible-light

photocatalytic activity for degradation of methyl orange (MO) and rhodamine B (RhB) dye. The reusability of the catalyst is evaluated by four consecutive catalytic runs.

## Experimental section

### Preparation of g-$C_3N_4$-M

The g-$C_3N_4$-M was synthesized by directly heating melamine according to a reported procedure.[25] Typically, 5 g of melamine was put into an alumina crucible with a cover, then heated at 773 K for 2 h at the rate of 2 K $min^{-1}$. Further heat treatment was performed at 793 K for another 2 h with the same heating rate. The resultant yellow powder was used in the subsequent studies.

### Preparation of g-$C_3N_4$-MN

The g-$C_3N_4$-M nanosheets were prepared by thermal exploitation of g-$C_3N_4$-M obtained above.[32] In a typical synthesis, 1g of g-$C_3N_4$-M placed in an open alumina crucible was heated at 793 K for 4 h at the rate of 2 K $min^{-1}$. A light yellow powder of g-$C_3N_4$-MN was obtained.

### Decoration of g-$C_3N_4$-MN with $Ag_2CO_3$ nanoparticles

The $Ag_2CO_3$/g-$C_3N_4$-MN photocatalysts were fabricated as follows: a certain amount of the as-prepared g-$C_3N_4$-MN was dispersed in 8 mL of deionized water and sonicated for 30 min. Then a solution of $AgNO_3$ (0.018 g, 2 mL) was added into the above suspension and stirred for 30 min in the dark to reach complete adsorption of $Ag^+$ on the surface of g-$C_3N_4$-MN. After that, 5 mL of $NaHCO_3$ solution (0.05M) was added into the above $Ag^+$-g-$C_3N_4$-MN suspension drop by drop. After stirring for 2 h, the precipitate was collected by centrifugation, washed with deionized water and ethanol, and dried at 333 K for 4 h. The $Ag_2CO_3$/g-$C_3N_4$-MN composites with different mass ratios were fabricated through changing the amount of g-$C_3N_4$-MN. The samples are denoted as MN-10, MN-20, MN-30 and MN-40 when the weight percentages of $Ag_2CO_3$ in $Ag_2CO_3$/g-$C_3N_4$-MN composites are 10%, 20%, 30%, 40%, respectively. The bare $Ag_2CO_3$ was synthesized by the same method without the addition of g-$C_3N_4$-MN suspension. The composite of M-30 (weight percentage of $Ag_2CO_3$ in $Ag_2CO_3$/g-$C_3N_4$-M is 30%) was also prepared by using g-$C_3N_4$-M instead of g-$C_3N_4$-MN.

### Characterization

Powder X-ray diffraction (XRD) analysis was determined by Siemens D5005 Diffractometer with Cu Kα radiation (λ = 1.5418 Å). Scanning electron microscopy (SEM) image and energy dispersive X-ray (EDX) spectrum were performed by using XL30 ESEM FEG microscope. Transmission electron microscopy (TEM) image was obtained on a JEM-2100F microscope with an accelerating voltage of 200 kV. X-ray photoelectron spectroscopy (XPS) was performed by using a Thermo ESCALAB 250 XPS instrument equipped with a standard and monochromatic source (Al Kα $h\upsilon$ = 1486.6 eV). The specific surface area of the samples was measured on a Micromeritics Tristar 3000 analyzer at 77.4 K. Photoluminescence (PL) spectra were obtained from FLSP920 Edinburgh Fluorescence Spectrometer. UV-vis diffuse reflectance spectroscopy (DRS) was collected through a Cary 500 spectrometer. The thermogravimetric analysis (TGA) was performed by the NETZSCH STA 449 F3 Jupiter instrument with a heating rate of 10 K $min^{-1}$ from room temperature to 1093 K under air flow.

### Photocatalytic Test

The photocatalytic performance of the samples was evaluated through the photodegradation of MO and RhB under visible light. A 300 W Xe lamp (Feilai Bo Technology Co., Ltd., China) combined with a 400 nm cut-off filter provided visible-light irradiation. In a typical photocatalytic measurement, suspension including the photocatalyst (30 mg) and MO or RhB solution (90 mL, 10 mg $L^{-1}$) was laid in a beaker. Before irradiation, the reaction suspension was ultrasonicated for 5 min and stirred in the dark for 30 min to reach adsorption-desorption equilibrium. During the photocatalytic tests, 3 mL of the suspension was obtained at a given time intervals, followed by centrifugation at 10000 rpm for 5 min to remove the photocatalyst. The degradation results were analyzed by using the UV–vis–NIR (Purkinje General, TU-1900) spectrophotometer.

## Results and Discussion

### Structure and property analysis

*In situ* growth strategy is widely used to prepare different kinds of composites such as graphene-based composite materials. In this work, $Ag_2CO_3$/g-$C_3N_4$-MN photocatalysts are fabricated by the *in situ* precipitation method at room temperature as shown in Scheme 1. Firstly, g-$C_3N_4$-M nanosheets obtained from the bulk g-$C_3N_4$-M through a thermal exploitation method are dispersed into deionized water by sonication. With the addition of $AgNO_3$ solution, $Ag^+$ can be bound tightly to the surface of g-$C_3N_4$-M nanosheets due to the chemical adsorption. Secondly, with the adding of $NaHCO_3$ solution, $Ag^+$ ions attached to the surface of g-$C_3N_4$-MN react with $HCO_3^-$ to generate $Ag_2CO_3$ nanoparticles under constant stirring. The g-$C_3N_4$-M nanosheet may act as an excellent substrate to hinder the aggregation of $Ag_2CO_3$ nanoparticles. Finally, $Ag_2CO_3$/g-$C_3N_4$-MN heterostructured photocatalysts are obtained.

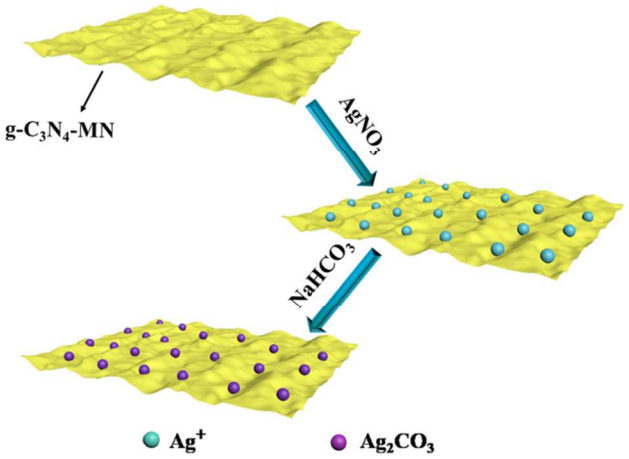


**Scheme 1** Schematic diagram of the fabrication of $Ag_2CO_3$/g-$C_3N_4$-MN composites.

The crystal structures of the as-prepared photocatalysts were examined by powder XRD. The supporting Fig. S1 shows that all the diffraction peaks of g-$C_3N_4$-M and g-$C_3N_4$-MN can be

indexed to the hexagonal phase of g-$C_3N_4$ (JCPDS 87-1526).[27] But the dominant peak related to the (0 0 2) interlayer reflection in g-$C_3N_4$-MN changes from 27.3° to 27.7°. This may be due to the decreased distance between the layers.[32] The small reflection peak relates to the in-plane structural packing motif at approximately 13° in g-$C_3N_4$-MN does not change greatly. As shown in Fig. 1, for the bare $Ag_2CO_3$ nanoparticles, all of the diffraction peaks can be readily indexed to monoclinic phase $Ag_2CO_3$ (JCPDS 26-0339). After coupled with $Ag_2CO_3$ nanoparticles, the composites of M-30 and MN-30 show the diffraction peaks of both g-$C_3N_4$ and $Ag_2CO_3$ phases, indicate that a coexistence of $Ag_2CO_3$ and g-$C_3N_4$, and no impurities are formed during the fabrication of the composites.

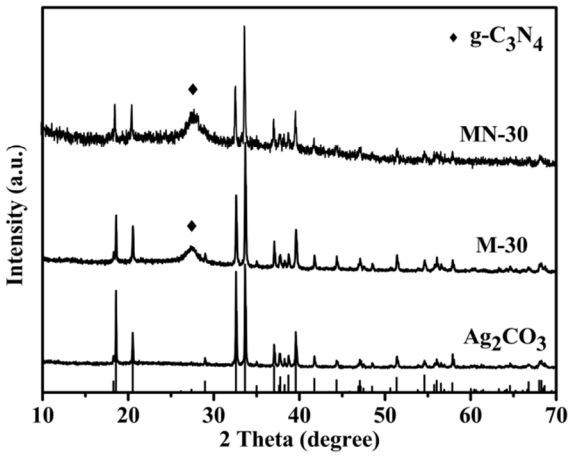


**Fig. 1** XRD patterns of as-prepared $Ag_2CO_3$, M-30 and MN-30 composites.

SEM images of g-$C_3N_4$-M and g-$C_3N_4$-MN are shown in Fig. 2A and 2B, respectively. It can be seen that both g-$C_3N_4$-M and g-$C_3N_4$-MN possess sheet structure. TEM images of g-$C_3N_4$-M and g-$C_3N_4$-MN are shown in Fig. 2C and 2D, respectively. Compared with g-$C_3N_4$-M, g-$C_3N_4$-MN becomes more flexible and its thickness decreases dramatically, which may result in the increase of the specific surface area and the reactive sites. As for the as-prepared nanocomposites, $Ag_2CO_3$ nanoparticles are found to be aggregating in M-30 (Fig. 2E). However, $Ag_2CO_3$ nanoparticles are highly dispersed on the surface of g-$C_3N_4$-MN and their sizes become much smaller (Fig. 2F, Fig. S2).

Fig. 3 shows the EDX spectrum and XPS spectra of the MN-30 composite. The EDX spectrum in Fig. 3A indicates that the composite is composed of C, N, O and Ag element, which is consistent with the result of XPS survey spectrum (Fig. 3B). The thermogravimetric analysis of MN-30 indicates that the weight percentage of $Ag_2CO_3$ in MN-30 composite are 32.0%, which is nearly consistent with the theoretical dosage (Fig. S3). The corresponding high-resolution XPS spectra are shown in Fig. 3C-F. The two individual peaks with the binding energies of 368.0 and 374.0 eV in Fig. 3C are ascribed to Ag $3d_{5/2}$ and Ag $3d_{3/2}$, respectively.[20,34,35] The high-resolution C 1s spectrum in Fig. 3D exhibits two main peaks at 284.6 and 288.1 eV. The peak at 284.6 eV can be attributed to carbon in $Ag_2CO_3$[34,35] or graphitic carbon in g-$C_3N_4$-MN.[36] Another peak at 288.1 eV can be identified as $sp^2$ C atoms that corresponds to N−C=N coordination in g-$C_3N_4$-MN. The main N 1s spectrum is shown in Fig. 3E. The peak at 398.5 eV is assigned to $sp^2$ hybridized aromatic N bonded to

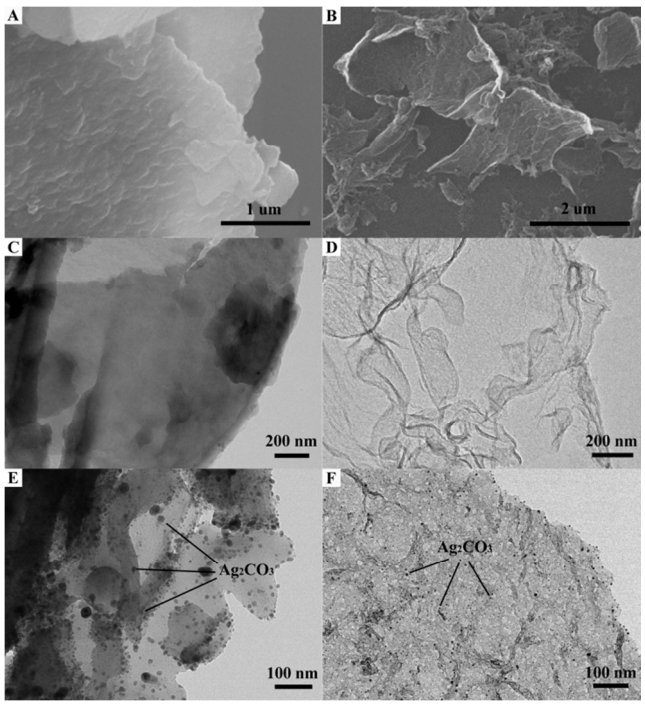


**Fig. 2** SEM images of (A) g-$C_3N_4$-M and (B) g-$C_3N_4$-MN. TEM images of (C) g-$C_3N_4$-M, (D) g-$C_3N_4$-MN, (E) M-30 and (F) MN-30 samples.

carbon atoms (C=N−C). The emergence of the peak at 400.1 eV corresponds to tertiary N bonded to C atoms in the form of N–$(C)_3$.[36] The weak peak at 401.1 eV is from the N-H structure. The O 1s peak shown in Figure 3F could be split into two peaks. The peak at 532.2 eV is assigned to the external –OH group or water species adsorbed on the surface of the sample. The other peak

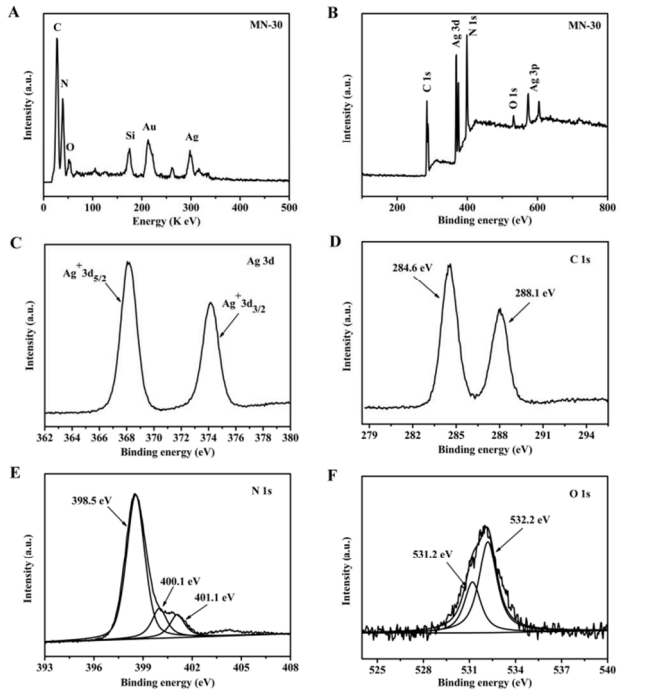


**Fig. 3** EDX spectrum (A) and XPS survey spectrum (B) of MN-30 composite.The corresponding high-resolution XPS spectra: (C) Ag 3d,

(D) C 1s, (E) N 1s and (F) O 1s.

appearing at 531.2 eV corresponds to oxygen in $Ag_2CO_3$, which is highly consistent with the value reported previously.[23,35]

Fig. 4 displays the nitrogen adsorption-desorption isotherms and the corresponding pore size distribution curves of the as-prepared g-$C_3N_4$-MN and MN-30 samples. It can be seen that both of them exhibit type *IV* isotherm and $H_3$-type hysteresis loop ($P/P_0$>0.4), thus implying the mesoporous features of the materials. As expected, the BET surface area of g-$C_3N_4$-MN is 155 $m^2$ $g^{-1}$, which is much higher than that of g-$C_3N_4$-M (10 $m^2$ $g^{-1}$, Fig. S4). After decoration with $Ag_2CO_3$ nanoparticles, the MN-30 composite still possesses a large surface area of 105 $m^2$ $g^{-1}$.

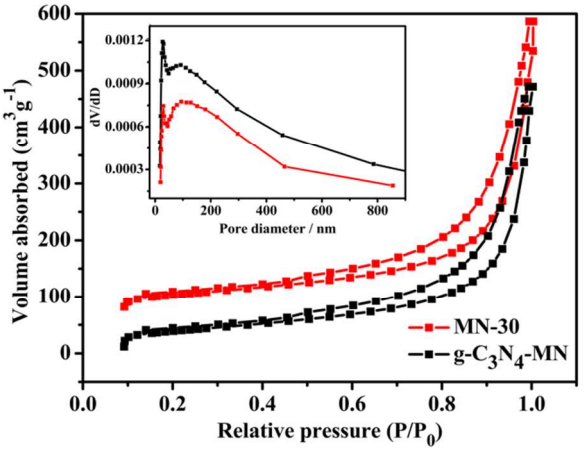


**Fig. 4** Nitrogen adsorption-desorption isotherms and the corresponding pore size distribution curves (inset) of the bare g-$C_3N_4$-MN and MN-30 composite.

PL technique is usually employed to investigate the migration, transfer and recombination processes of photogenerated electron-hole pairs in semiconductors. As shown in Fig. 5, both the bare g-$C_3N_4$-M and g-$C_3N_4$-MN have a strong, wide peak in PL spectra. However, the PL peaks of M-30 and MN-30 composites decrease remarkably, and the peak in the PL spectrum of MN-30 is very weak, indicating the recombination of electron-hole pairs in MN-30 is hindered greatly.

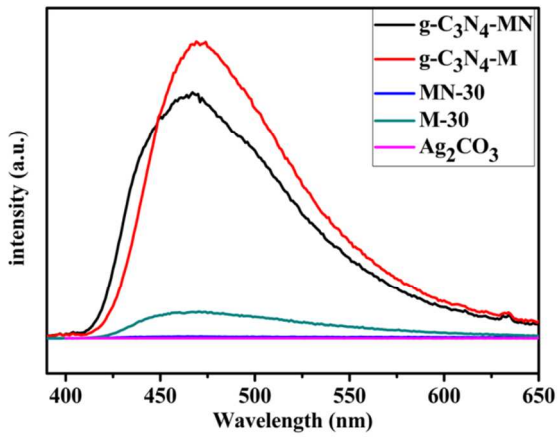


**Fig. 5** Photoluminescence spectra of the as-prepared photocatalysts.

The light absorption properties of the as-prepared samples were investigated by UV–vis DRS. As shown in Fig. 6, g-$C_3N_4$-MN shows a slight blue shift of absorption edge compared to g-$C_3N_4$-M, which is similar to the performance of other g-$C_3N_4$ nanosheet fabricated by heating dicyandiamide.[32] Notably, the $Ag_2CO_3$/g-$C_3N_4$-MN composites show a significant enhancement of light absorption, and the absorption intensity increases with the increasing amounts of $Ag_2CO_3$. In addition, based on the plot of transformed Kubelka-Munk function $(F(R)h\upsilon)^n$ versus the energy of exciting light ($h\upsilon$) (n value is 2 for direct transition and 1/2 for indirect transition, Fig. S5),[23,32] the bandgap of g-$C_3N_4$-M, g-$C_3N_4$-MN and $Ag_2CO_3$ is estimated to be 2.64, 2.67 and 2.37 eV, respectively.

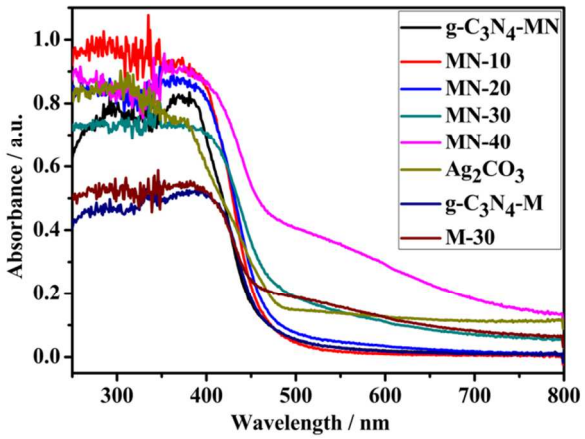


**Fig. 6** UV–vis diffuse reflectance spectra of the as-prepared photocatalysts.

**Photocatalytic activity**

Fig. 7A and 7B show the photocatalytic activities of the as-prepared samples and commercial P25 catalyst toward degradation of MO under visible-light irradiation (λ > 400 nm). As shown in Fig. 7A, no obvious degradation of MO is observed after visible light irradiation for 30 min in the absence of catalysts, indicating that the photolysis of MO can be ignored. Compared to pure $Ag_2CO_3$ and g-$C_3N_4$-MN, all $Ag_2CO_3$/g-$C_3N_4$-MN composites exhibit enhanced photocatalytic activities and the photocatalytic activities increases gradually as increasing the proportion of $Ag_2CO_3$ in the composites. The as-prepared MN-30 composite shows the highest activity and no enhancement is observed with further increasing the $Ag_2CO_3$ content up to 40%. The results above indicate that the amount of $Ag_2CO_3$ in the composite is crucial to the synergistic effect between the two components.[37,38] Additionally, the photocatalytic activities of g-$C_3N_4$-M, M-30 composite and commercial P25 were also tested for comparison under the same conditions. As shown in Fig. 7B, they all show rather poor photocatalytic activity for the degradation of MO compared to the MN-30 photocatalyst.

RhB was also selected as the other target compound to further evaluate the photocatalytic activity of MN-30 composite. Fig. 7C shows that almost all RhB is degraded for MN-30 after 30 min visible-light irradiation. But only 7.4%, 11.3%, 26.7%, 33.1% and 41.2% of RhB is removed under the same conditions for P25, g-$C_3N_4$-M, M-30, $Ag_2CO_3$ and g-$C_3N_4$-MN, respectively. The results of degradation of MO and RhB dyes confirm that the large surface area and the small sheet thickness of the g-$C_3N_4$-MN

substrate may play an important role for improving photocatalytic performance.

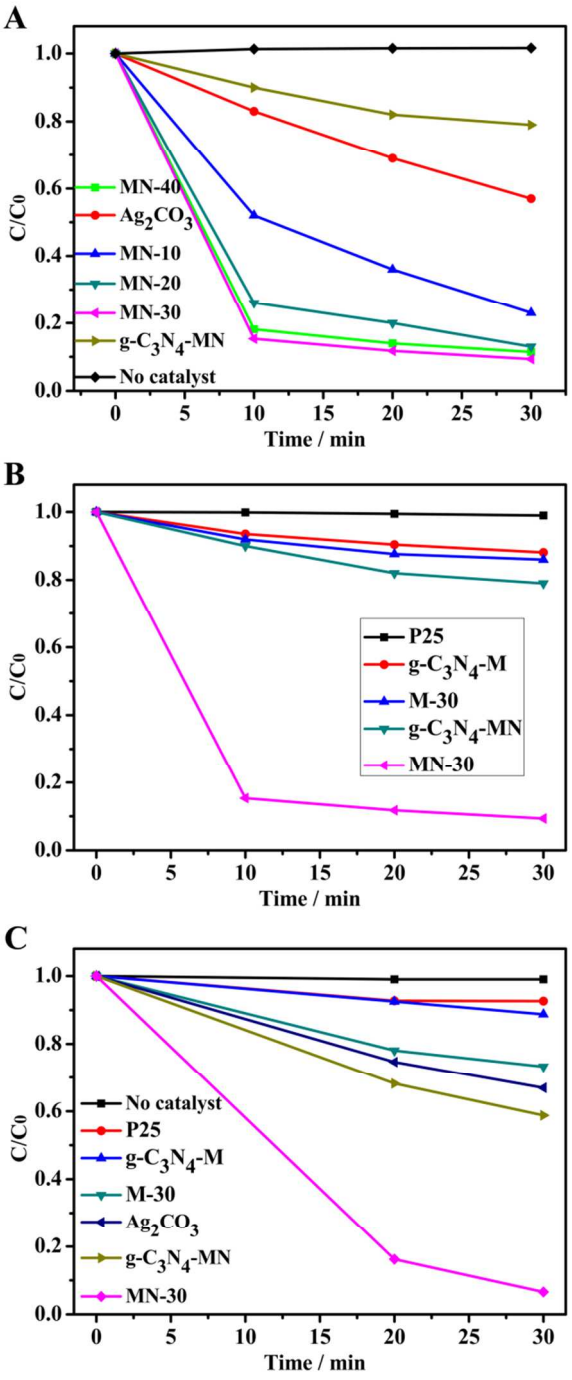


**Fig. 7** Photocatalytic activity of as-prepared samples and commercial P25 catalyst toward degradation of MO (A) and (B), RhB (C) under visible light irradiation.

### Catalyst Stability

From the viewpoint of practical applications, the stability of the bare $Ag_2CO_3$ and MN-30 samples was also investigated. Fig. 8 shows that a relatively high stability is kept over the MN-30 heterostructured photocatalyst during the successive cycle of photocatalytic degradation of MO, whereas $Ag_2CO_3$ nanoparticles almost lose their activity in the second run due to the photocorrosion. g-$C_3N_4$ possesses a conjugated π structures, which has been proven to effectively suppress photocorrosion during the g-$C_3N_4$ based photocatalytic reaction.[39,40] It is notable that the photocatalytic efficiency of MN-30 composite does not exhibit any significant loss of activity even after four successive cycles, indicating its excellent stability and great potential value in environmental purification.

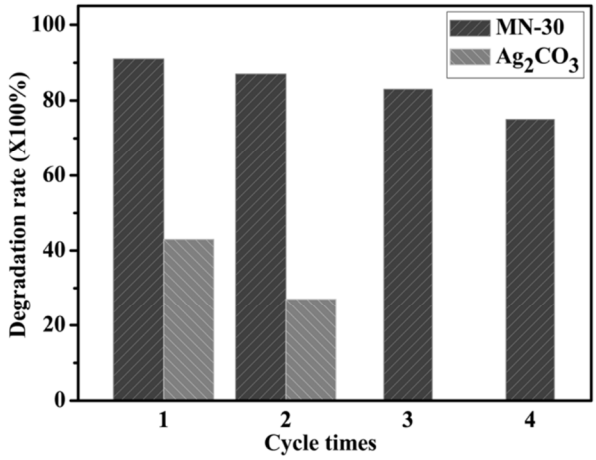


**Fig. 8** The reusability of as-prepared $Ag_2CO_3$ and MN-30 composite for photodegradation of MO.

### Possible Photocatalytic Mechanism

It is important to investigate possible photocatalytic mechanism for a composite photocatalyst system. In this study, the trapping experiments of free radical and hole are carried out to investigate the main reactive species for degradation of MO and RhB by MN-30. Disodium ethylenediaminetetraacetate (EDTA), 1,4-benzoquinone (BQ) and tert-butyl alcohol (*t*-BuOH) are used as the hole scavenger, superoxide radical ($\cdot O_2^-$) scavenger and hydroxyl radical (·OH) scavenger, respectively. The results (Fig. S6) show that the degradation rate of MO is decelerated obviously after addition of 2 mM EDTA or 2 mM BQ. However, the degradation rate has almost no change in the presence of *t*-BuOH, suggesting that the holes and $\cdot O_2^-$ are the main reactive species for degradation of MO. As for the degradation of RhB, the photocatalytic activity decreases slightly after addition of *t*-BuOH, however it is inhibited greatly in the presence of EDTA and BQ, indicating that the holes and $\cdot O_2^-$ also play a major role in the degradation of RhB.

Based on the above experimental results and physicochemical properties of g-$C_3N_4$-MN and $Ag_2CO_3$, a possible photocatalytic mechanism of $Ag_2CO_3$/g-$C_3N_4$-MN system is proposed. Photo-excited carriers can transfer smoothly mainly due to the matching potentials of the composites, as shown in Fig. 9. The band gap of g-$C_3N_4$-MN and $Ag_2CO_3$ is 2.67 eV and 2.37 eV, respectively. Thus both the g-$C_3N_4$-MN and $Ag_2CO_3$ can be excited under the visible light radiation. The g-$C_3N_4$-MN has a more negative potential of the conduction band (CB: ~-1.1 eV) and valence band (VB: ~1.6 eV)[38,41] than that of $Ag_2CO_3$ (CB: ~0.3 eV, VB: ~2.7 eV, see the Supporting Information). Therefore, the excited electrons on g-$C_3N_4$-MN could directly inject into the CB of $Ag_2CO_3$, meanwhile the holes could migrate from the VB of $Ag_2CO_3$ to that of g-$C_3N_4$-MN, which promotes the effective separation of photoexcited electrons and holes. As a result, the

enriched electrons on the CB of $Ag_2CO_3$ will react with oxygen to generate superoxide radicals ($\cdot O_2^-$). The $\cdot O_2^-$ active species together with the holes on the VB of g-$C_3N_4$-MN are responsible for the degradation of organic pollutants.

After one cycle of photodegradation reaction, the $Ag^0$ nanoparticles were formed on the surface of $Ag_2CO_3$ (Fig. S7), which generally serve as a good electron acceptor. Therefore, the electrons on the CB of $Ag_2CO_3$ can transfer to the $Ag^0$ nanoparticles, which may decreases the amount of $\cdot O_2^-$ that generated on the CB of $Ag_2CO_3$. This may cause the decreased photocatalytic activity in recycling reactions. The enriched electrons on the $Ag^0$ nanocrystals could react with oxygen via multielectron-transfer routes ($O_2+2e^-+2H^+=H_2O_2$; $O_2+4e^-+4H^+=2H_2O$).[22,28] Moreover, the Ag nanoparticles gradually grew on the $Ag_2CO_3$ surface under the photocatalytic reaction process, which could prevent the light absorption of $Ag_2CO_3$[31]. In addition, the excessive $Ag^0$ could become the recombination center of electrons and holes,[42] which also resulting in the decreased of the photocatalytic activity.

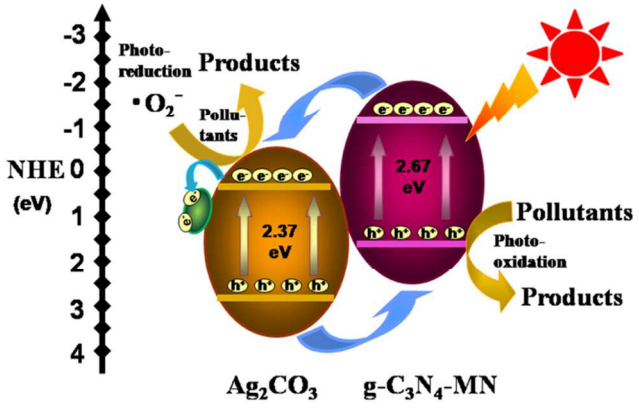


**Fig. 9** Schematic illustration of photocatalytic reaction and charge transfer of the $Ag_2CO_3$/g-$C_3N_4$-MN composites under visible-light irradiation.

## Conclusion

In summary, g-$C_3N_4$-M nanosheets (g-$C_3N_4$-MN) have been prepared through a thermal exploitation process from its parent bulk material, and the novel g-$C_3N_4$-M nanosheets loaded with highly-dispersed $Ag_2CO_3$ nanoparticles were fabricated at room temperature. Under visible light irradiation, the $Ag_2CO_3$/g-$C_3N_4$-MN heterostructures show much superior photocatalytic activities to the $Ag_2CO_3$/g-$C_3N_4$-M (bulk g-$C_3N_4$) composites and the pure $Ag_2CO_3$ nanoparticles. The enhanced photocatalytic activity of the $Ag_2CO_3$/g-$C_3N_4$-MN composites was mainly attributed to the large surface area and the small sheet thickness of the g-$C_3N_4$-MN substrate, as well as the improved dispersibility and the decreased particle size of $Ag_2CO_3$. The $Ag_2CO_3$/g-$C_3N_4$-MN composite may serve as a promising candidate as the catalytic material in pollution treatment applications.

## Acknowledgements

This work is supported by the National Natural Science Foundation of China (Grant No. 21473027); The project development plan of science and technology of Jilin Province (No. 20140101110JC); Research Fund for the Doctoral Program of Higher Education of China (No. 20120043110005); Opening Fund of State Key Laboratory of Rare Earth Resource Utilization, Changchun Institute of Applied Chemistry, Chinese Academy of Sciences; Opening Fund of State Key Laboratory of Inorganic Synthesis and Preparative Chemistry of Jilin University.

## Notes and references

[a] *Department of Chemistry, Northeast Normal University, Changchun, 130024, China. E-mail: xingy202@nenu.edu.cn Tel:+86-431-85099657.*
[b] *State Key Laboratory of Rare Earth Resource Utilization, Changchun Institute of Applied Chemistry, Chinese Academy of Sciences, Changchun, 130022, P.R. China.*

†Electronic Supplementary Information (ESI) available: Other information of the samples. See DOI: 10.1039/b000000x/

1 M. R. Hoffmann, S. T. Martin, W. Choi and D. W. Bahnemann, *Chem. Rev.*, 1995, **95**, 69-96.
2 A. Kudo and Y. Miseki, *Chem. Soc. Rev.*, 2009, **38**, 253-278.
3 M. D. Hernández-Alonso, F. Fresno, S. Suárez and J. M. Coronado, *Energy Environ. Sci.*, 2009, **2**, 1231-1257.
4 G. Liu, Y. N. Zhao, C. H. Sun, F. Li, G. Q. Lu and H. M. Cheng, *Angew. Chem. Int. Ed.*, 2008, **47**, 4516-4520.
5 X. B. Chen and S. S. Mao, *Chem. Rev.*, 2007, **107**, 2891-2959.
6 D. Chen and J. H. Ye, *Adv. Funct. Mater.*, 2008, **18**, 1922-1928.
7 G. C. Xi, Y. Yan, Q. Ma, J. F. Li, H. F. Yang, X. J. Lu and C. Wang, *Chem. Eur. J.*, 2012, **18**, 13949-13953.
8 N. Z. Bao, L. M. Shen, T. Takata and K. Domen, *Chem. Mater.*, 2008, **20**, 110-117.
9 Y. X. Li, Y. F. Hu, S. Q. Peng, G. X. Lu and S. B. Li, *J. Phys. Chem. C*, 2009, **113**, 9352-9358.
10 G. C. Xi and J. H. Ye, *Chem. Commun.*, 2010, **46**, 1893-1895.
11 G. S. Li, D. Q. Zhang and J. C. Yu, *Chem. Mater.*, 2008, **20**, 3983-3992.
12 H. F. Cheng, B. B. Huang, Y. Y. Liu, Z. Y. Wang, X. Y. Qin, X. Y. Zhang and Y. Dai, *Chem. Commun.*, 2012, **48**, 9729-9731.
13 S. M. Sun, W. Z. Wang and L. Zhang, *J. Mater. Chem.*, 2012, **22**, 19244-19249.
14 Y. Zhang, B. Deng, T. R. Zhang, D. M. Gao and A. W. Xu, *J. Phys. Chem. C*, 2010, **114**, 5073-5079.
15 H. Yang and Z. H. Liu, *Cryst. Growth Des.*, 2010, **10**, 2064-2067.
16 M. Feng, M. Zhang, J. M. Song, X. G. Li and S. H. Yu, *ACS Nano*, 2011, **5**, 6726-6735.
17 H. Wang, J. Gao, T. Q. Guo, R. M. Wang, L. Guo, Y. Liu and J. H. Li, *Chem. Commun.*, 2012, **48**, 275-277.
18 Y. P. Bi, S. X. Ouyang, N. Umezawa, J. Y. Cao and J. H. Ye, *J. Am. Chem. Soc.*, 2011, **133**, 6490-6492.
19 Z. G. Yi, J. H. Ye, N. Kikugawa, T. Kako, S. X. Ouyang, H. Stuart-Williams, H. Yang, J. Y. Cao, W. J. Luo, Z. S. Li, Y. Liu and R. L. Withers, *Nat. Mater.*, 2010, **9**, 559-564.
20 H. J. Dong, G. Chen, J. X. Sun, C. M. Li, Y. G. Yu and D. H. Chen, *Appl. Catal., B*, 2013, **134-135**, 46-54.
21 C. W. Xu, Y. Y. Liu, B. B. Huang, H. Li, X. Y. Qin, X. Y. Zhang and Y. Dai, *Appl. Surf. Sci.*, 2011, **257**, 8732-8736.
22 G. P. Dai, J. G. Yu and G. Liu, *J. Phys. Chem. C*, 2012, **116**, 15519-15524.
23 C. L. Yu, G. Li, S. Kumar, K. Yang and R. C. Jin, *Adv. Mater.*, 2014, **26**, 892-898.
24 X. C. Wang, K. Maeda, A. Thomas, K. Takanabe, G. Xin, J. M. Carlsson, K. Domen and M. Antonietti, *Nat. Mater.*, 2009, **8**, 76-80.
25 S. C. Yan, Z. S. Li and Z. G. Zou, *Langmuir*, 2009, **25**, 10397-10401.
26 Y. X. Yang, Y. N. Guo, F. Y. Liu, X. Yuan, Y. H. Guo, S. Q. Zhang, W. Guo and M. X. Huo, *Appl. Catal., B*, 2013, **142-143**, 828-837.
27 L. Ge, C. C. Han, J. Liu and Y. F. Li, *Appl. Catal., A*, 2011, **409-410**, 215-222.
28 M. Xu, L. Han and S. J. Dong, *ACS Appl. Mater. Interfaces*, 2013, **5**, 12533-12540.

29 J. Cao, Y. J. Zhao, H. L Lin, B. Y. Xu and S. F. Chen, *Mater. Res. Bull.*, 2013, **48**, 3873-3880.
30 H. Katsumata, T. Sakai, T. Suzuki and S. Kaneco, *Ind. Eng. Chem. Res.*, 2014, **53**, 8018-8025.
31 H. Xu, Y. X. Song, Y. H. Song, J. X. Zhu, T. T. Zhu, C. B. Liu, D. X. Zhao, Q. Zhang and H. M. Li, *RSC Adv.*, DOI: 10.1039/C4RA03443K.
32 P. Niu, L. L. Zhang, G. Liu and H. M. Cheng, *Adv. Funct. Mater.*, 2012, **22**, 4763-4770.
33 H. X. Zhao, H. T. Yu, X. Quan, S. Chen, Y. B. Zhang, H. M. Zhao and H. Wang, *Appl. Catal., B*, 2014, **152-153**, 46-50.
34 H. J. Dong, G. Chen, J. X. Sun, Y. J. Feng, C. M. Li, G. H. Xiong and C. Lv, *Dalton Trans.*, 2014, **43**, 7282-7289.
35 H. Xu, J. X. Zhu, Y. X. Song, W. K. Zhao, Y. G. Xu, Y. H. Song, H. Y. Ji and H. M. Li, *RSC Adv.*, 2014, **4**, 9139-9147.
36 Y. J. Cui, J. S. Zhang, G. G. Zhang, J. H. Huang, P. Liu, M. Antonietti and X. C. Wang, *J. Mater. Chem.*, 2011, **21**, 13032-13039.
37 Y. S. Xu and W. D. Zhang, *ChemCatChem*, 2013, **5**, 2343-2351.
38 H. Xu, J. Yan, Y. G. Xu, Y. H. Song, H. M. Li, J. X. Xia, C. J. Huang and H. L. Wan, *Appl. Catal., B*, 2013, **129**, 182-193.
39 Y. J. Wang, R. Shi, J. Lin and Y. F. Zhu, *Energy Environ. Sci.*, 2011, **4**, 2922-2929.
40 S. Kumar, T. Surendar, A. Baruah and V. Shanker, *J. Mater. Chem. A*, 2013, **1**, 5333-5340.
41 S. W. Cao, Y. P. Yuan, J. Fang, M. M. Shahjamali, F. Y. C. Boey, J. Barber, S. C. J. Loo and C. Xue, *Int. J. Hydrogen Energy*, 2013, **38**, 1258-1266.
42 R. Georgekutty, M. K. Seery and S. C. Pillai, *J. Phys. Chem. C*, 2008, **112**, 13563-13570.